PROCEEDINGS, 51st Workshop on Geothermal Reservoir Engineering
Stanford University, Stanford, California, February 9-11, 2026
SGP-TR-229

Coupled DFN-Based Hydro-Mechanical Modeling of Hydraulic Stimulation in the Utah FORGE Reservoir

Matthew McLean[1, *], Hafssa Tounsi[1], Branko Damjanac[1], Zorica Radakovic-Guzina[1], Wei Fu[1], Pengju Xing[2], Aleta Finnila[3], Robert Podgorney[4]

[1] Itasca Consulting Group, Inc., Minneapolis, MN, USA

[2] Energy & Geoscience Institute, University of Utah, Salt Lake City, UT, USA

[3] WSP USA Inc., Redmond, WA, USA

[4] Idaho National Laboratory, Idaho Falls, ID, USA

[*] mmclean@oneitasca.com

Keywords: Discrete Fracture Network (DFN), Enhanced Geothermal System (EGS), Hydraulic Fracturing (HF), Numerical Modeling, Hydro-Mechanical Coupling.

ABSTRACT

Seismic and fiber-optic monitoring at the Utah FORGE site during the 2024 stimulation and circulation tests has enabled a refined characterization of the subsurface fracture network. The resulting discrete fracture network (DFN) provides improved constraints on fracture distribution, orientation, and connectivity. This study incorporates this refined DFN to perform a coupled hydro-mechanical analysis of the 2024 hydraulic stimulation using the discrete element method (DEM) based software XSite.

To constrain fracture mechanical and hydraulic properties, a systematic sensitivity analysis is first conducted using Stage 1 of the 2022 hydraulic stimulation. Key DFN, hydraulic, and mechanical parameters are varied to identify parameter combinations that best reproduce both the observed injection pressure response and the recorded microseismicity. The sensitivity analysis demonstrates that the system's response to fluid injection is highly influenced by the DFN realization and that the best match to field measurements is obtained by assuming an initially impermeable DFN with moderate shear strength which generally reproduces the extent of microseismic events and injection pressure history.

The calibrated modeling framework is then applied to stimulation Stages 8–10 of the 2024 campaign to assess the influence of DFN geometry and fracture hydraulic behavior on pressure response, fracture activation, and flow path development. The results confirm that an initially strong and impermeable DFN provides a better match to field observations, whereas weak and permeable DFN scenarios overestimate the spatial extent of fracture reactivation due to their diffuse response. While the updated DFN captures aspects of the observed stimulation behavior, particularly shear failure extent, more realistically in Stages 8 and 9, discrepancies remain near Stage 10, indicating missing fracture pathways or uncertainties in local fracture properties.

These findings highlight the importance of integrating geophysical data into DFN-based models to enhance their predictive capability and optimize reservoir development strategies in naturally fractured geothermal systems.

1. INTRODUCTION

Hydraulic stimulation at the Utah Frontier Observatory for Research in Geothermal Energy (FORGE) site was conducted to increase fracture connectivity and permeability between injection well 16A(78)-32 and production well 16B(78)-32. In 2022, well 16A(78)-32 underwent a three-stage hydraulic stimulation, including one open-hole stage near the toe (Stage 1) and two stages in cased intervals (Stages 2 and 3). In 2024, a commercial-scale multi-stage stimulation campaign was carried out in the same well, including re-stimulation of the 2022 intervals and stimulation of additional perforated sections (Stages 4 to 10), followed by circulation tests between the two wells. All campaigns were monitored using bottomhole pressure measurements, microseismic monitoring (Dyer et al., 2024, Niemz et al., 2025), with distributed fiber-optic sensing additionally deployed during the 2024 campaign. A fiber optic DAS cable, cemented behind the casing of well 16B(78)-32, recorded strain variations during the stimulation from injection well 16A(78)-32. Large strain changes were identified as potential fracture intersections with the production well.

The numerical modeling efforts to reproduce the observed pressure response and microseismicity at the Utah FORGE site, demonstrated that the system response is strongly controlled by the geometry and connectivity of the discrete fracture network (DFN) and its mechanical and hydraulic properties (Xing et al., 2023, Ghassemi et al., 2025, Podgorney et al., 2025, Tounsi et al., 2025, Xing et al., 2025). Seismic and distributed fiber-optic monitoring acquired during the 2024 stimulation and circulation tests have enabled a refined characterization of the subsurface fracture network, providing improved constraints on fracture distribution, orientation, and connectivity. As a result, the DFN geometry has been progressively updated to reflect field observations (Finnila, 2021, Finnila and Jones 2024, Finnila, 2025). However, despite these advances, the mechanical and hydraulic properties of fractures within the DFN remain poorly constrained,

introducing significant uncertainty into coupled hydro-mechanical simulations and limiting the capability of existing models to interpret field data and serve as predictive tools.

The paper is structured in three parts. The first part provides a brief overview of the numerical modeling approach and describes the model setup, assumptions, and material properties.

In the second part, a systematic sensitivity analysis is conducted using Stage 1 of the 2022 hydraulic stimulation. Key DFN, hydraulic, and mechanical parameters are varied to identify parameter combinations that best reproduce both the observed injection pressure response and the recorded microseismicity.

In the third part, the calibrated modeling framework is applied to Stages 8, 9 and 10 of the 2024 stimulation. Stages 8 and 9 involved multi-cluster injection configurations and therefore represent more complex stimulation conditions, whereas Stage 10 corresponds to a single-cluster injection. Simulated pressure evolution, fracture activation, and microseismic patterns during these stages are compared with field observations, including bottomhole pressure and seismic monitoring data. For this comparison, the recorded wellhead treating pressure is converted to bottomhole pressure by accounting for hydrostatic and frictional wellbore losses (Xing et al., 2023).

2. NUMERICAL MODELING METHODOLOGY

2.1 Numerical Model

To analyze the different stimulation stages, we performed coupled hydro-mechanical simulations of fluid injection and hydraulic fracture propagation in a naturally fractured reservoir using XSite, a Discrete Element Method (DEM) code developed by Itasca Consulting Group (Itasca, 2023). XSite employs the Synthetic Rock Mass (SRM) method and a lattice numerical approach to model deformation, hydraulic fracture propagation, and related microseismicity in naturally fractured reservoirs. Its capabilities have been verified for viscosity-dominated and toughness-dominated hydraulic fracturing regimes and the interaction of hydraulic fractures with existing fractures (Damjanac and Cundall, 2016; Fu et al., 2016, 2019). The thermal effects were not considered in this study because they were deemed insignificant for the injection durations.

2.1 Model Setup

The model simulates a fractured granitic rock volume with dimensions of 600 m × 600 m × 600 m, rotated by 25° from the N-S direction to align with the principal stress directions. It is centered around the analyzed stimulation stages and encompasses the stimulated volume between the injection well and the production well. Rock and fluid properties and in-situ stress magnitudes are summarized in Table 1. The analysis focuses on stimulation of Stages 1, 8, 9, and 10, which span a range of injection configurations and operational conditions. Stages 8 and 9 involved multi-cluster injection and therefore represent more complex stimulation conditions, whereas Stages 1 and 10 correspond to single-cluster injections. Table 2 summarizes the key operational parameters for the analyzed stages, including the number of clusters, cluster spacing, pumping fluid, maximum pumping rate, and depth. The well trajectories for 16A(78)-32 and 16B(78)-32 were incorporated into the model geometry, though near-wellbore fracture initiation and perforation effects, as described by Fu et al. (2024), were not explicitly modeled. Perforation clusters were represented as spherical zones, with fracturing initiated from circular startup joints of 4 m radius. Six perforations were assumed to actively take fluid for each cluster. Pressure drop across the perforation tunnels in well 16A(78)-32 was considered in the multi-cluster stages only (Stages 8 and 9). Stages 8, 9, and 10 were modeled in sequence to account for stress shadow effects during stimulation. Subdomains were created around the analyzed stages, with a 2 m lattice resolution that gradually increased to 12 m in the main domain.

Table 1: Rock properties and initial conditions.

Parameter	**Schistose Quartzite**	
Young's modulus, GPa	55	
Poisson's ratio	0.26	
Tensile Strength, MPa	10	
Fracture toughness, MPa.m$^{1/2}$	3	
Fluid viscosity, cP	Slickwater	2
	Linear Gel	25
Pore pressure, MPa/m	0.00981	
Minimum horizontal stress gradient, MPa/m	0.017 – Dip Direction N115°E	
Maximum horizontal stress gradient, MPa/m	0.02 - Dip Direction N25°E	
Vertical stress gradient, MPa/m	0.026	

Table 2: Field pumping information for the five analyzed stimulation stages.

Stage name	Number of clusters	Clusters spacing (m)	Pumping fluid	Maximum pumping rate (bpm)	Measured Depth (m)
Stage 1	1	-	Slickwater	50	3,288 - 3,349 (10,787 - 10,987 ft)
Stage 8	8	7.6 (25 ft)	XL CMHPG	80	2,910 – 2,963 (9,547 - 9,722 ft)
Stage 9	8	7.6 (25 ft)	Slickwater	80	2,841 – 2,895 (9,322 - 9,497 ft)
Stage 10	1	-	Slickwater	35	2,826 (9,272 ft)

3. SENSITIVITY ANALYSIS AND MODEL CALIBRATION USING STAGE 1 STIMULATION DATA

3.1 Previous Modeling Efforts

In April of 2022, three stages of stimulation were carried out during the initial large-scale stimulation campaign in well 16A(78)-32 at the Utah FORGE site (McLennan et al., 2023). This was part of a multi-stage stimulation treatment: Stage 1 at the open hole section toward the toe of the well (10,787 ft md), followed by Stages 2 and 3 in shallower, cased intervals. Simulation of stage 1 had a maximum injection rate of 50 bpm with a total injection volume of 4,261 bbl of slickwater (Figure 1). Wellhead pressure, injection rate, and microseismic events were recorded during the field stimulations with geophones in multiple offset wells.

The original modeling efforts focused on matching simulation results of Stages 1 to 3 to field data in three areas: (1) injection pressure history, (2) spatial distribution and magnitude of microseismic events, and (3) the Gutenberg–Richter b-value (the slope of the magnitude–frequency distribution). The detailed analysis and results of this model are presented in Xing et al. (2023) and will be briefly summarized in the following. The original models used a stochastic DFN based on the interpretation of a Formation Micro Imager (FMI) log (Finnila, 2021). A portion of this DFN realization in the vicinity of Stage 1 is shown in Figure 1. This model investigated the impact of mechanical and hydraulic properties of the DFN on stimulation. The key results of original modeling efforts indicated that a weak and in-situ permeable DFN yields the best match to the field observations compared to a strong and impermeable DFN. The weak DFN corresponds to natural fractures with purely frictional strength, i.e., without cohesive or tensile strength. The strong DFN corresponds to natural fractures with frictional and cohesive strength, representative of a cemented fracture without in-situ permeability. Figure 1 shows that the model with a weak and permeable DFN closely matches the observed injection pressure history, especially at later times. The early-time response is controlled more by near-wellbore effects, including fracture initiation and tortuosity, which this field-scale model does not capture (Fu et al., 2024). The model with a strong and impermeable DFN, however, overestimates injection pressure by more than 500 psi when the injection rate reaches the maximum of 50 bpm.

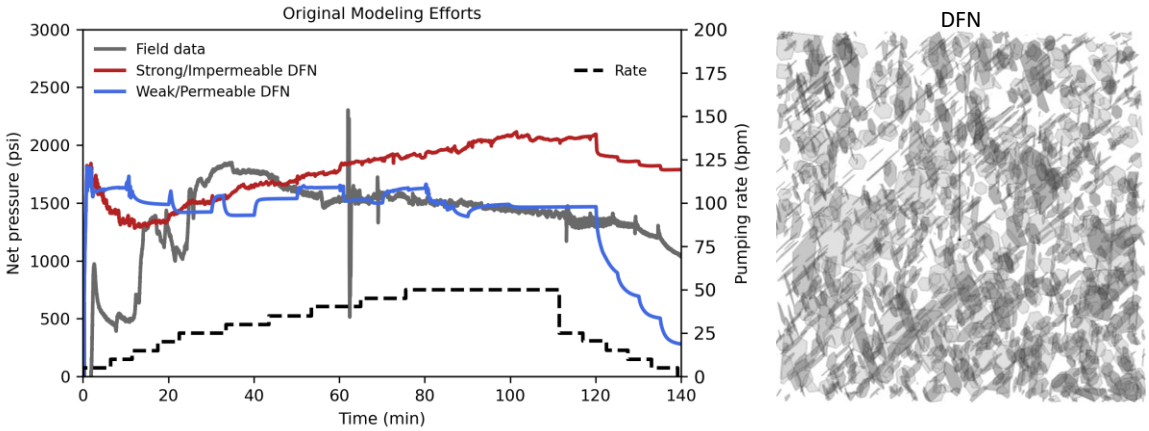

Figure 1: (Left) measured and predicted pumping rate and bottomhole pressure histories in Stage 1. (Right) Stochastic DFN in the vicinity of Stage 1.

Furthermore, the model incorporating a weak and permeable DFN reproduces the spatial extent of observed microseismic events in the field (Figure 2). This model predicts a mixed stimulation mechanism of natural fracture shear reactivation and propagation of tensile fractures. Yet, assuming a strong and in-situ impermeable DFN results in predominantly propagation of tensile fractures optimally oriented perpendicular to the minimum principal stress (Figure 2). The observed spatial distribution of microseismic events produced by stimulation of Stage 1 does not support purely tensile fracture propagation. In summary, the original modeling efforts for Stages 1-3 concluded that a DFN with purely frictional strength and in-situ permeability provided the best fit to field data.

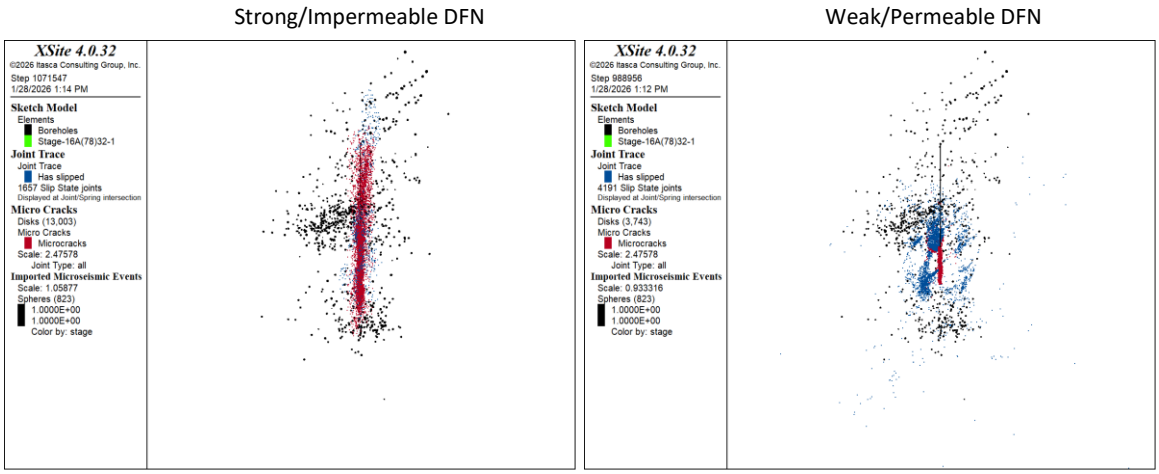

Figure 2: Comparison of the location of measured and predicted microseismic events spatial distribution for Stage 1.

Subsequent modeling efforts focused on the 2024 hydraulic stimulation campaign for Stages 4–10 (Tounsi et al., 2025a). These efforts investigated the impact of DFN mechanical and hydraulic properties on stimulation, similar to the original efforts for Stages 1-3. The DFN utilized in the model for Stages 4-10 included 17,855 stochastically generated fractures and refined with additional fractures to match the microseismic events recorded during stimulation (Finnila and Jones, 2024). The key results of this model indicated that (1) the in-situ permeability of nature fractures has a large impact on injection pressure and fluid migration and (2) a strong DFN (frictional and cohesive strength) without in-situ permeability best approximated the observed injection pressure history (Tounsi et al., 2025b). The model reproduces key field observations, including injection pressure history and fracture growth patterns.

3.2 Results and Discussion

Building on previous efforts that used different realizations of the DFN and required different assumptions and properties to reproduce field observations, this section aims to establish a unified set of properties that can best reproduce the field measurements. This analysis takes the original model for Stage 1 as a starting point, incorporates the latest 2025 v1 DFN (Finnila, 2025), and investigates the impact of DFN hydraulic and mechanical properties on hydraulic stimulation. The cases considered for sensitivity analysis are shown in Table 3, which include two cases with an in-situ impermeable DFN (different strengths) and two cases with a permeable DFN (different fracture stiffness). Due to the uncertainty in the magnitude and distribution of natural fracture strength and stiffness, the chosen ranges are intended to span the expected variability. The initial DFN hydraulic apertures utilized in the following are in the range of 0.02 to 0.1 mm.

Table 3: Modeling cases for sensitivity analysis of stage 1 with 2025 v1 DFN.

Case	Friction (°)	Cohesion (MPa)	Tension (MPa)	In-situ permeable	Normal/Shear stiffness (GPa/m)
A	37	20	10	No	20/20
B	37	10	5	No	20/20
C	37	0	0	Yes	20/20
D	37	0	0	Yes	100/100

The sensitivity analysis of Stage 1 with a refined natural fracture characterization shows that using similar DFN properties to the original modeling efforts results in low injection pressure compared to field measurements (Figure 3). Injection pressure is underestimated by more than 1,000 psi with a weak and initially permeable DFN with moderate joint stiffness. Consequently, incorporating additional field measurements to refine fracture characterization may result in a previously calibrated model no longer reproducing observations. Increasing the natural fracture stiffness (with all else equal) results in a better match to the observed injection pressure history (Figure 3). However, as discussed below, the spatial distribution of DFN shear reactivation increases significantly. Given these results, we also explore the impact of natural fracture strength on stimulation for an initially impermeable DFN. The analysis shows that the modeling cases with moderate DFN strength provide a better match between measured and predicted injection pressure history, especially in later times (Figure 4). A very strong DFN that is initially impermeable tends to overestimate injection pressure history by more than 1,000 psi when the injection rate reaches the maximum of 50 bpm.

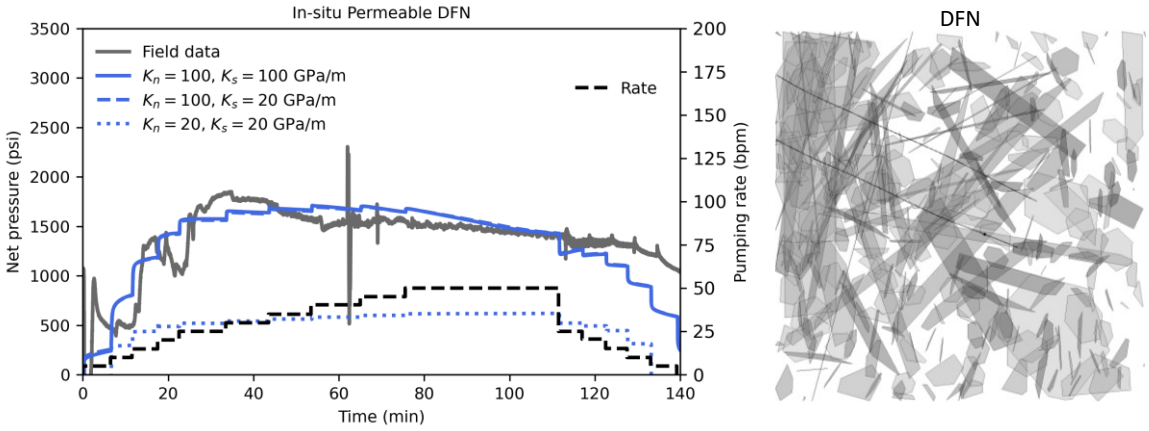

Figure 3: (Left) measured and predicted pumping rate and bottomhole pressure histories in Stage 1 for models with an initially permeable DFN. (Right) The 2025 v1 DFN in the vicinity of Stage 1.

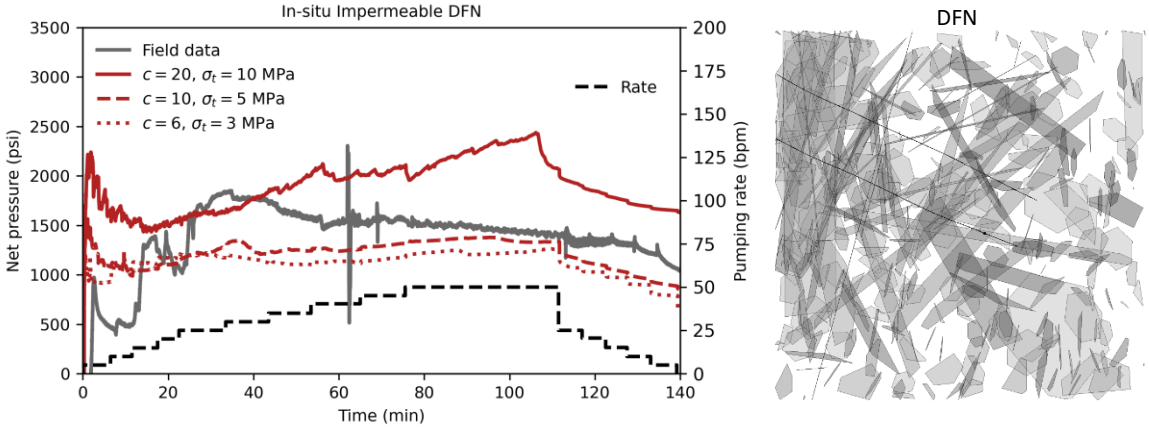

Figure 4: (Left) measured and predicted pumping rate and bottomhole pressure histories in Stage 1 for models with an initially impermeable DFN. (Right) The 2025 v1 DFN in the vicinity of Stage 1.

The stimulation mechanism and extent of tensile/shear failure are shown for all Stage 1 modeling cases in Figure 5. The results indicate that DFN mechanical and hydraulic properties strongly influence the stimulation mechanism and extent of stimulation. A strong and impermeable DFN (Case A) results in mostly tensile failure aligning perpendicular to the least principal stress, i.e., a vertical hydraulic fracture in the normal faulting regime. The hydraulic fracture propagates until it intersects a sub-vertical natural fracture and subsequently arrests. Fluid injection past this point results in shear reactivation of the DFN. The observed spatial distribution of microseismicity in field measurements does not support this stimulation mechanism. The initially impermeable DFN with reduced strength (Case B) results in mostly shear reactivation along the DFN (Figure 5). In this case, tensile failure is localized near the injection point; however, with increasing distance from the source, the dominant stimulation mechanism transitions to shear reactivation. Although discrepancies remain in the predicted extent and locations of shear slip events, the impermeable DFN with reduced strength reproduces the general extent of observed events. Conversely, the weak and initially permeable DFN models (Cases C and D) do not reproduce the extent of observed microseismic events. The permeable DFN results in a highly diffusive response that leads to natural fracture shear reactivation far from the injection point.

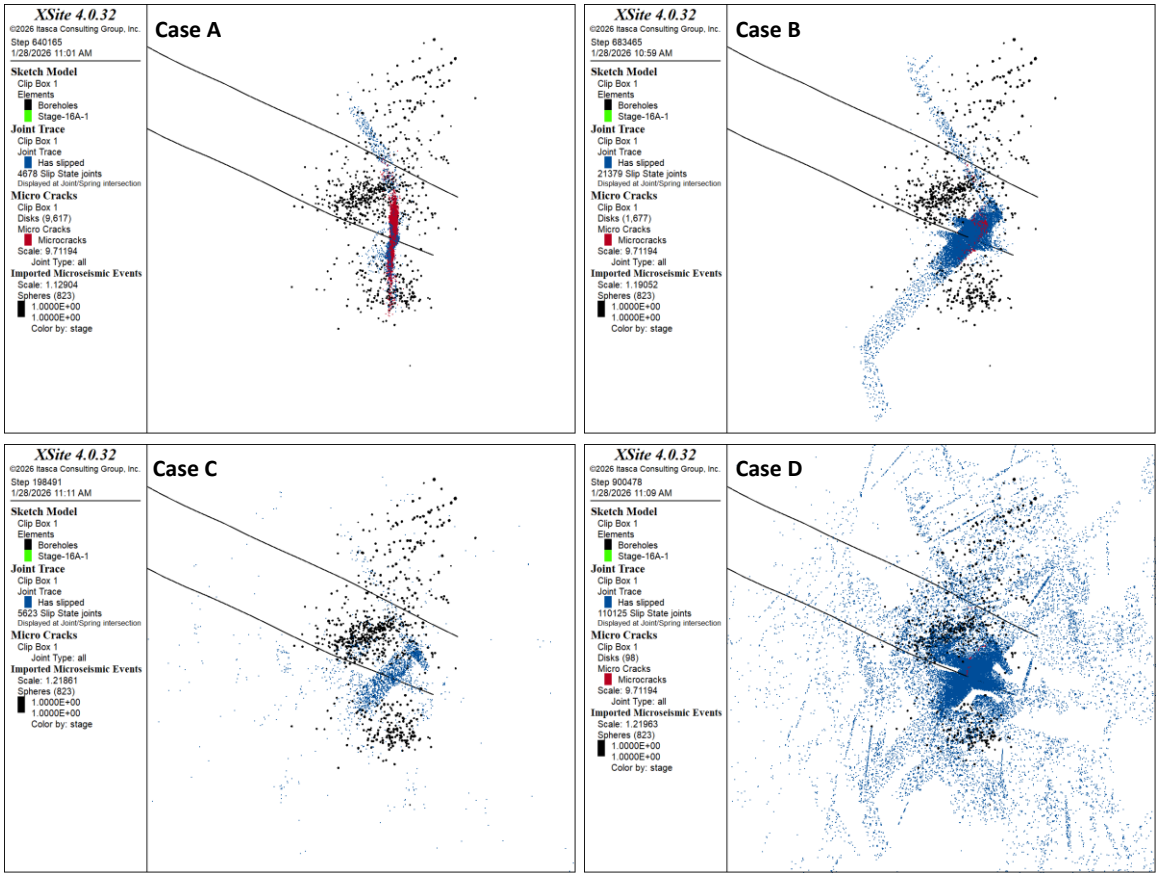

Figure 5: Comparison of measured and predicted microseismic spatial distribution for Stage 1 with the 2025 v1 DFN.

The hydraulic aperture distribution near the open-hole section and at the end of injection for Stage 1 is shown in Figure 6. The impermeable DFN cases with shear strength show injection fluid localization in hydraulic fractures and a few reactivated natural fractures. Many natural fractures near Stage 1 do not reactivate or open and, hence, remain with low apertures. The initially permeable DFN cases, however, result in hydraulic aperture increase in a large extent from the injection point as fluid diffuses into the permeable fractures. Apertures are smallest for Case C, driven mostly by low injection pressure. Increasing natural fracture stiffness results in larger apertures and promotes deeper fluid penetration into the system.

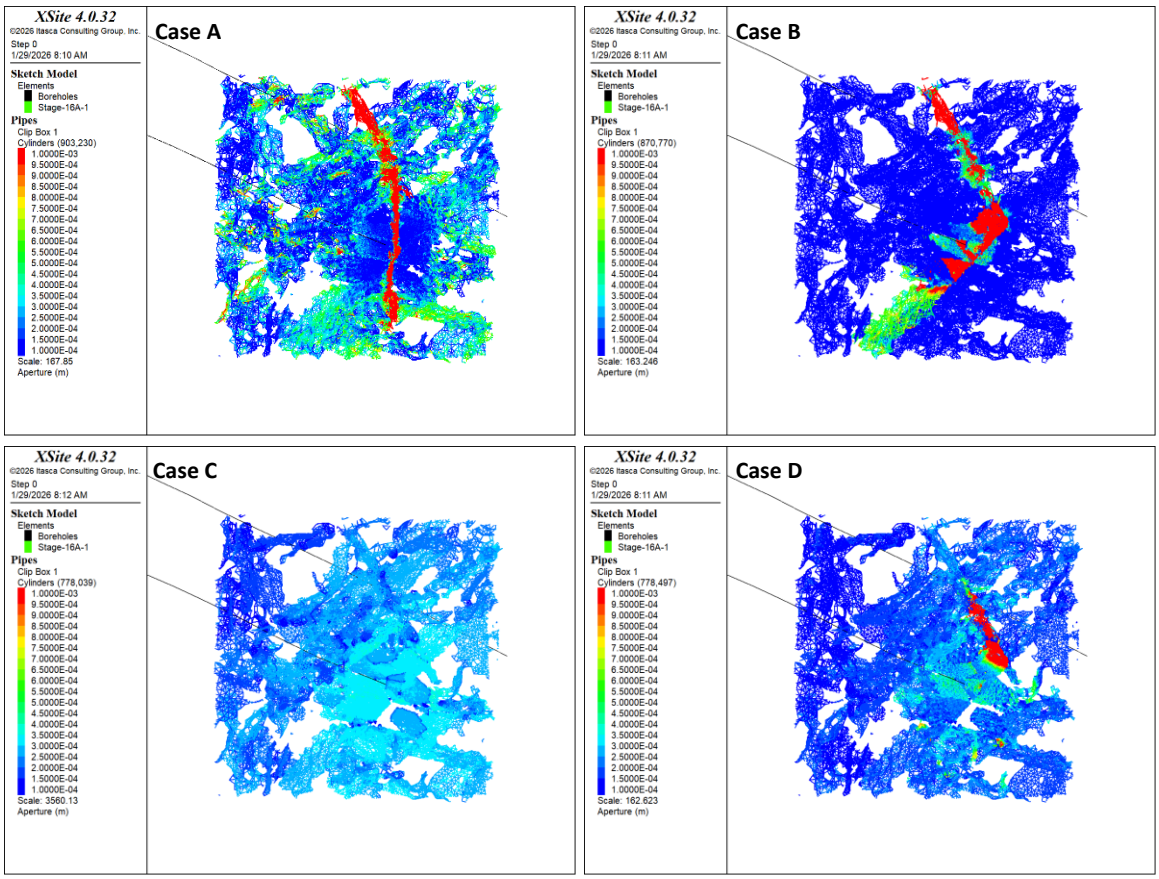

Figure 6: Aperture (m) distribution for stimulation of Stage 1 with the 2025 v1 DFN.

3.3 Summary of Sensitivity Analysis

This sensitivity analysis concludes that (1) the predicted stimulation mechanism and the system's response to fluid injection is highly influenced by the DFN realization, particularly the fracture network's spatial distribution, density, and connectivity, (2) initially permeable DFN with large stiffness can reproduce the observed injection pressure history but tends to overestimates the extent the fracture reactivation events due to a highly diffusive response, (3) initially impermeable DFN with large shear strength results in mostly tensile fracture propagation and localization of failure oriented perpendicular to minimum principal stress; this does not reproduce observed microseismic event spatial location nor injection pressure history, and (4) the best match of field measurements is obtained for the initially impermeable DFN with moderate shear strength, which generally reproduces the extent of microseismic events and injection pressure history.

4. APPLICATION TO THE 2024 MULTI-STAGE STIMULATION (STAGES 8-10)

In this section, the calibrated modeling framework is applied to the 2024 multi-stage stimulation, focusing on Stages 8–10. Simulations are performed using both the 2024 DFN realization and the newly developed 2025 v1 DFN realization. For each DFN realization, two fracture hydraulic property cases are considered: a strong impermeable DFN case (Case A; Table 3) and a weak permeable DFN (Case C; Table 3). In both cases, the joint normal stiffness and joint shear stiffness are fixed at 20 GPa/m. This controlled comparison is designed to isolate the influence of DFN geometry and connectivity, as well as fracture hydraulic behavior, on modeled pressure evolution and fracture opening and slip. The hydraulic fractures from Stages 3, 4 and 6 as defined by Finnila (2025) were also included in the model and assumed to be permeable and frictional in all scenarios.

4.1 2024 and 2025 v1 DFN realizations

The 2024 and 2025 v1 DFN realizations differ in fracture size distribution, density, and connectivity as a result of the additional datasets used to constrain the 2025 v1 DFN. In the 2024 DFN, most fractures were stochastically generated and iteratively updated using microseismic data from April 2022 stimulation (Finnila et al., 2021; Finnila and Jones, 2024). This DFN includes 17,854 natural fractures with equivalent radii ranging from 13 m to 170 m and an average equivalent radius of 28 m. The 2025 v1 DFN was constructed using microseismic data from both April 2022 stimulation and the 2024 stimulation and circulation tests (Finnila, 2025). It comprises 19,537 stochastic fractures with equivalent radii ranging from 11.6 m to 149.1 m (average 28.4 m), together with 126 discrete fractures with equivalent radii ranging from 14.3 m to 748.9 m (average 146.5 m). Figure 7 illustrates the differences between the 2024 and 2025 v1 DFN realizations in the vicinity of Stages 8–10.

Moreover, the 2024 DFN did not include a representation of the west-dipping natural fault (F2) that was later identified as a major location of microseismic activity during Stages 8–10 (Ajo-Franklin et al., 2025). In the 2025 v1 DFN, this structure was incorporated based on reflection imaging and microseismic observations, together with additional connecting natural fractures in the vicinity of the stimulated interval (Figure 7).

Initial fracture hydraulic apertures were calibrated by Finnila and Jones (2024), based on bulk rock porosity (1-2%) and a fracture aperture-size relationship of the form $e = \alpha R_e^{\beta}$, where R_e is the equivalent fracture radius, $\alpha = 5 \times 10^{-5}$ and $\beta = 0.5$. This relationship is widely used in the literature to describe aperture-length scaling, with reported values spanning $\alpha \in [7e-4, 1.16]$ and $\beta \in [0.22, 0.69]$ based on field observations (Klimczak et al., 2010). Previous modeling at the FORGE site indicated that the original parameterization produced fracture apertures that were larger than implied by observed pressure responses, motivating a reduction of the parameter α to 5×10^{-6} (Tounsi et al., 2025). In the 2025 v1 DFN, fractures in the region of interest are larger on average than in the 2024 DFN, and applying the same aperture–size relationship would further increase initial apertures. To maintain consistency between DFN realizations, the value of α was therefore further reduced in the 2025 v1 DFN by a factor of 0.5, such that the maximum initial fracture aperture (0.065 mm) is the same in both realizations. Figure 8 shows the relationship between fracture aperture and equivalent radius for the 2024 DFN realization and for the 2025 v1 DFN, both with and without application of the 0.5 scaling factor on the parameter α.

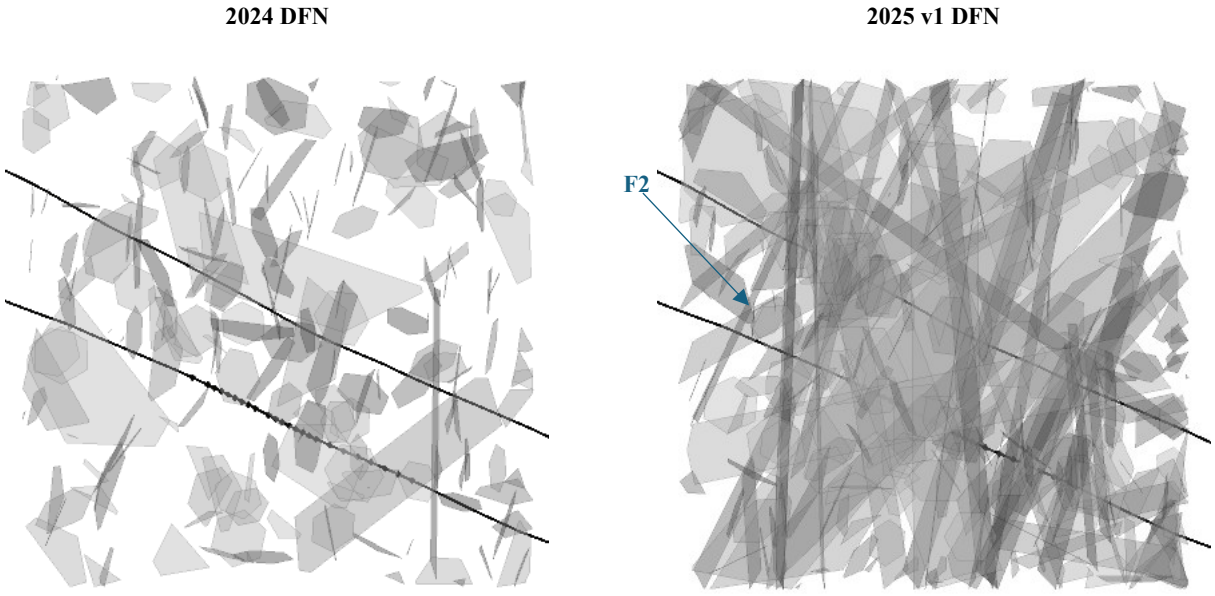

Figure 7: Comparison of the two DFN realizations in the vicinity of Stages 8-10.

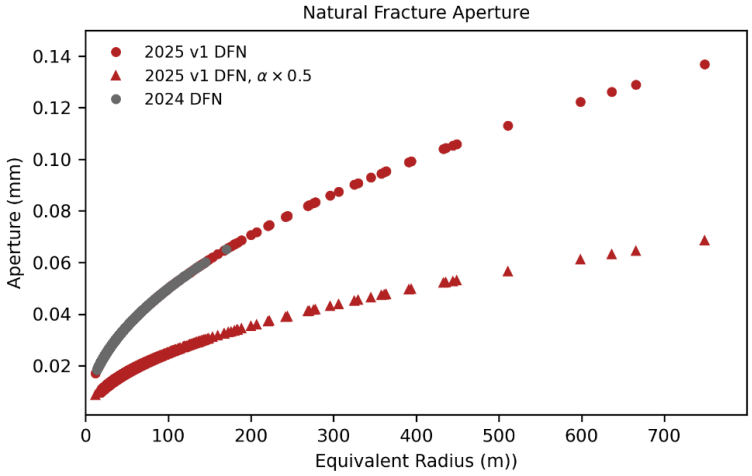

Figure 8: Fracture aperture versus equivalent radius for the 2024 DFN realization and the 2025 v1 DFN, with and without application of the 0.5 scaling factor to the parameter α.

4.2 Results and Discussion

Figures 9, 10 and 11 show the pumping rate and bottomhole injection pressure histories for Stages 8, 9, and 10, respectively. For each stage, the measured field data are plotted together with simulation results obtained using the 2024 DFN and the 2025 v1 DFN realizations under both strong/impermeable and weak/permeable DFN assumptions.

In Stage 8, none of the scenarios reproduce the early-time pressure evolution observed in the field data, likely reflecting near-wellbore and thermal effects not included in the simulations. During the steady pumping phase, the impermeable DFN scenarios show the best agreement with the observed pressure response, whereas the permeable DFN scenarios underestimate the pressure. This underestimation is more pronounced for the 2025 v1 DFN, which has a denser and more connected fracture network, allowing injected fluid to be distributed into a larger fracture volume and resulting in lower pressure buildup.

In Stage 9, the field pressure history is inconsistent with the expected hydraulic response, suggesting uncertainty in the pressure data for this stage. The simulation results exhibit trends similar to those observed in Stage 8. Impermeable DFN scenarios produce higher pressures of comparable magnitude for both DFN realizations, whereas permeable DFN scenarios significantly underestimate pressure, particularly for the 2025 v1 DFN.

Stage 10 exhibits a pressure response that differs from Stages 8 and 9 and is indicative of the formation of a dominant hydraulic fracture. This behavior is closely reproduced by the impermeable DFN scenario using the 2024 DFN realization. In contrast, simulation using the 2025 v1 DFN shows a pronounced pressure increase, suggesting interaction with a natural fracture that acts as a barrier to hydraulic fracture propagation.

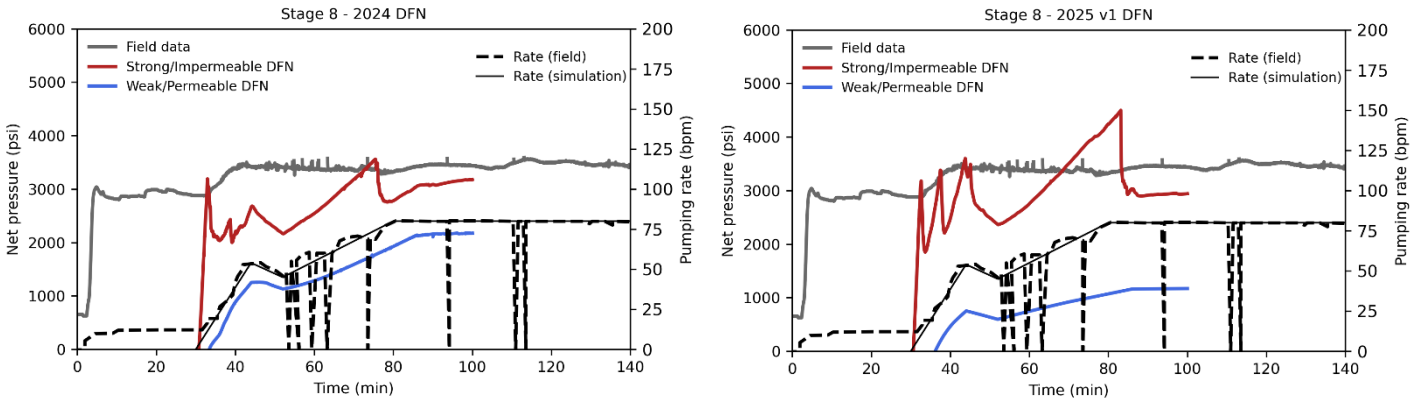

Figure 9: Measured and predicted pumping rate and bottomhole pressure histories in Stage 8 using the 2025 v1 DFN (right) and the 2024 DFN (left).

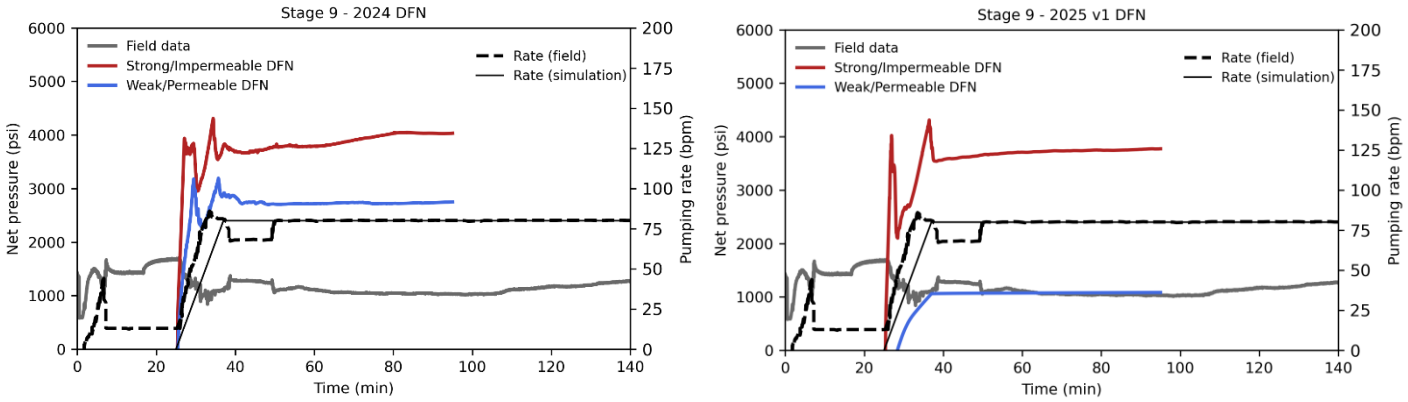

Figure 10: Measured and predicted pumping rate and bottomhole pressure histories in Stage 9 using the 2025 v1 DFN (right) and the 2024 DFN (left).

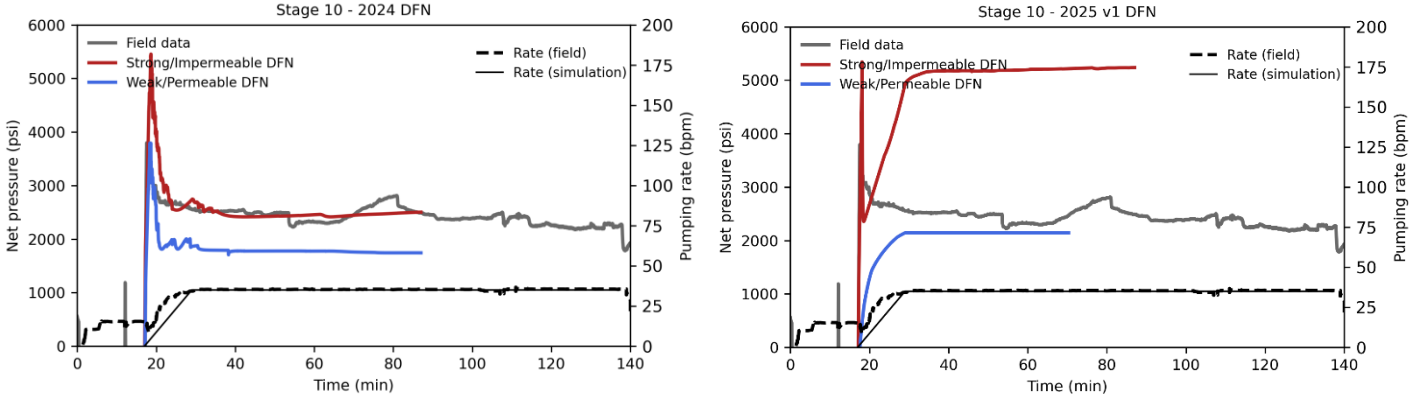

Figure 11: Measured and predicted pumping rate and bottomhole pressure histories in Stage 10 using the 2025 v1 DFN (right) and the 2024 DFN (left).

The stimulation mechanism and spatial extent of tensile and shear failure at the point reached in the simulations during Stage 10, are shown in Figure 12 for both DFN realizations and for both initial DFN permeability scenarios. In the 2025 v1 DFN, shear reactivation is the dominant stimulation mechanism in both the impermeable and permeable cases, with tensile failure being nearly absent in the permeable scenario. In contrast, the 2024 DFN, which is less dense and characterized by smaller fracture sizes, exhibits markedly different behavior. In the impermeable case, tensile failure is the dominant stimulation mechanism, whereas in the permeable case shear reactivation becomes dominant, with tensile failure still present, unlike in the 2025 v1 DFN.

In the 2024 DFN impermeable scenario, three distinct stimulation-induced flow paths develop and connect to the production well. One is nearly perpendicular to the deviated wellbores, while the other two initially propagate in a sub-vertical way and subsequently dip toward the heel of the well as they intersect natural fractures. These well-defined flow paths are difficult to identify in the plots of the other scenarios, where increased DFN density and size distribution or permeability promote more spatially diffuse shear reactivation.

Microseismic events recorded in the field during Stages 8–10 (Dyer et al., 2024) are also shown in Figure 12. None of the simulated scenarios reproduces the observed concentration of microseismicity along Fault F2. This outcome is expected for the 2024 DFN, as Fault F2 was not included in that realization. In the 2024 DFN impermeable case, simulated shear events are primarily concentrated above the interval stimulated in stages 8–10. In contrast, simulations using the 2025 v1 DFN show a more diffuse shear event distribution that dips toward the heel of the well and is spatially closer to the location of Fault F2. The permeable DFN cases exhibit unrealistically diffuse deformation patterns, suggesting that the placement of far-field model boundaries may influence these results and should be extended in future simulations.

It should be noted that the simulations are computationally intensive, particularly because Stages 8–10 were modeled sequentially. Consequently, the constant-rate injection period was not fully modeled. Future work will extend the simulations to cover the entire injection schedule in order to evaluate the potential for reactivation of Fault F2 during continued injection.

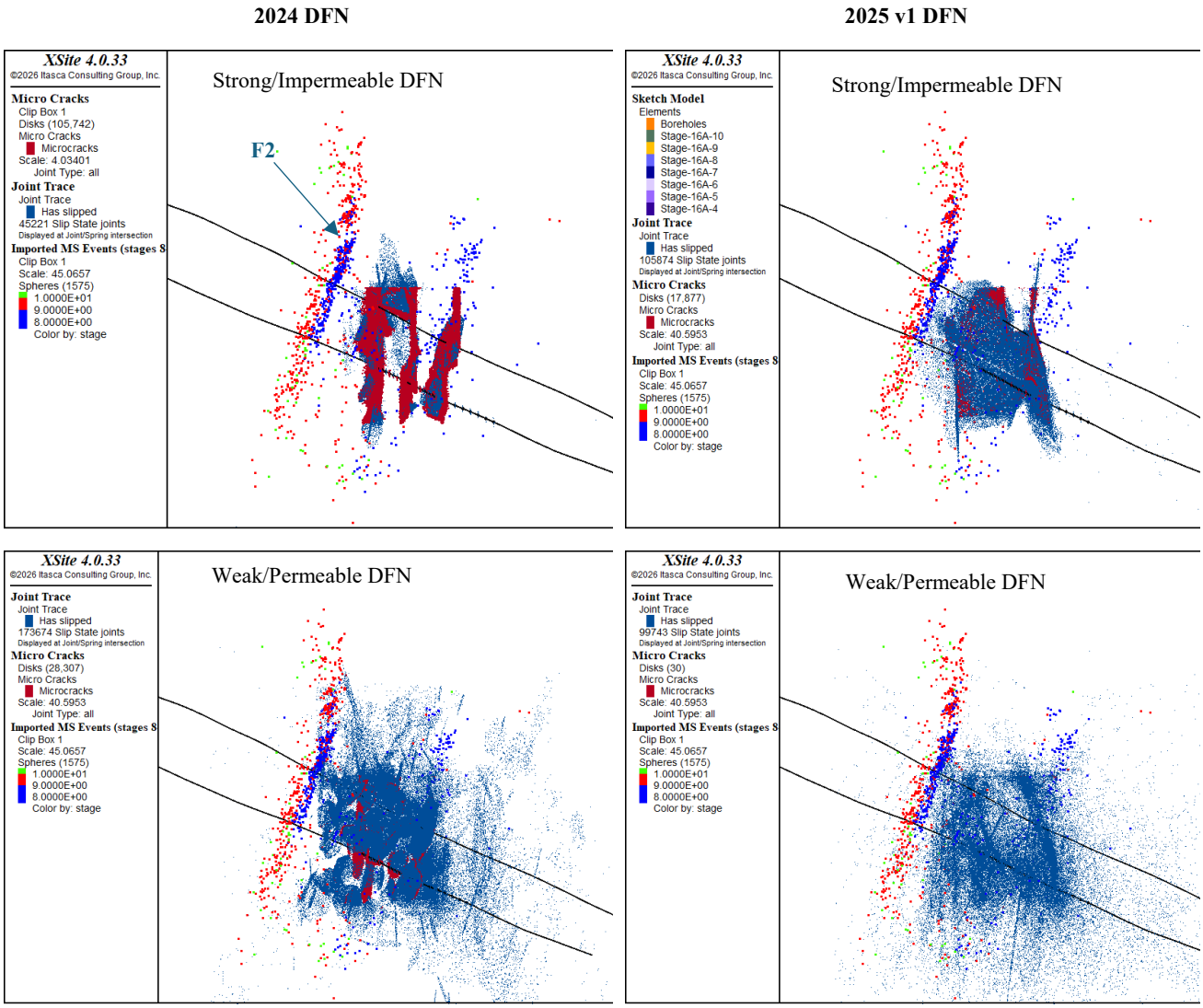

Figure 12: Comparison of measured and predicted microseismic spatial distribution for stages 8–10 using the 2024 DFN (left) and the 2025 v1 DFN (right).

The aperture distribution in the vicinity of the clusters of stages 8–10 at the point reached in the simulations during Stage 10, are shown in Figure 13 for both DFN realizations and for both initial DFN permeability scenarios. In the initially impermeable DFN scenarios, distinct flow paths connecting the injection and production wells are clearly visible. In contrast, fracture reactivation in the permeable DFN scenarios is spatially diffuse, making it difficult to identify dominant flow paths. The permeable 2025 v1 DFN scenario exhibits the smallest fracture apertures among all cases, consistent with the lower injection pressures predicted for this scenario.

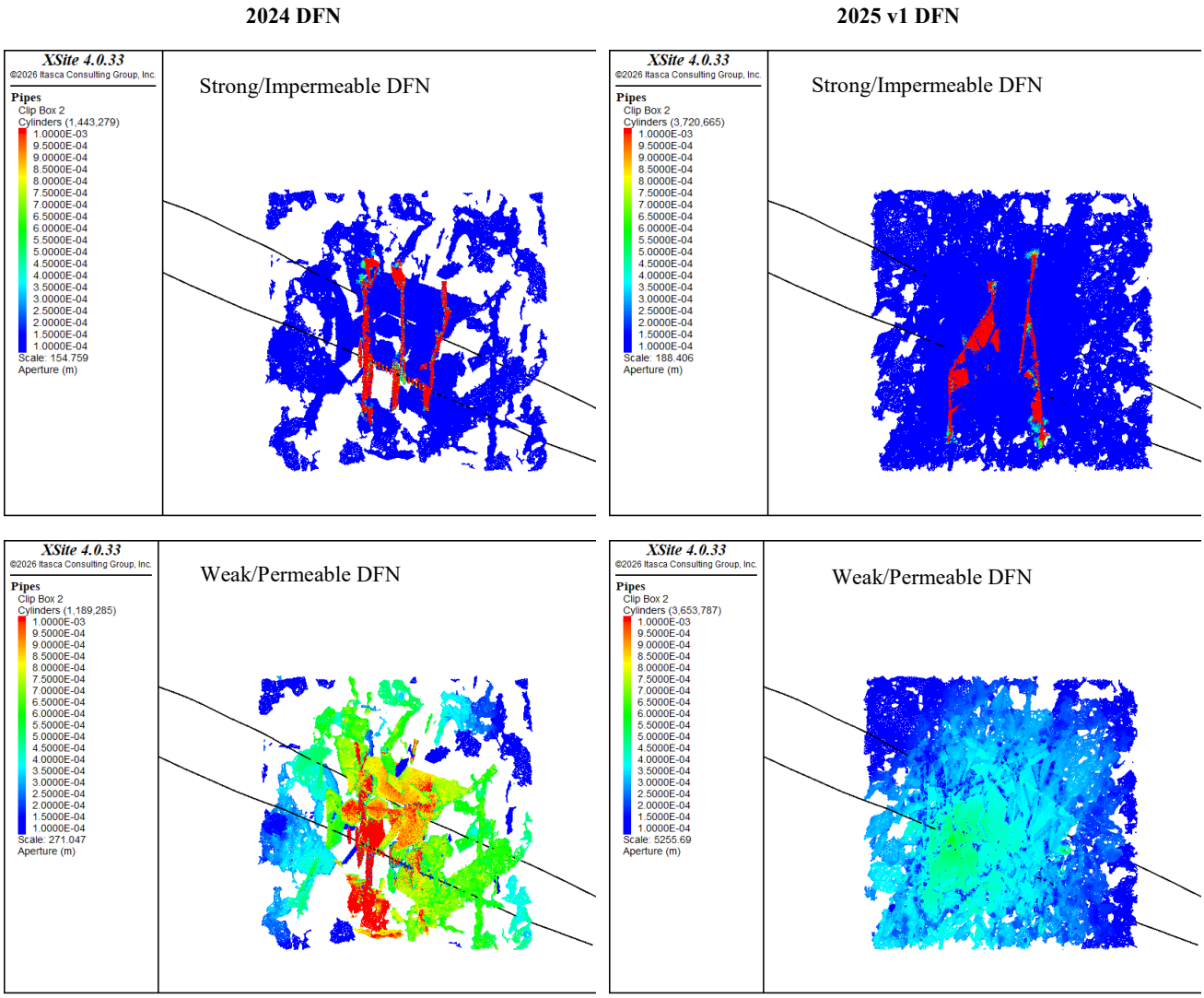

Figure 13: Aperture (m) distribution at the simulated state reached during Stage 10 using the 2024 DFN (left) and the 2025 v1 DFN (right).

For the impermeable scenarios, the 2024 DFN predicts three stimulation-induced flow paths connecting the injection and production wells, whereas the 2025 v1 DFN predicts two. The absence of this third flow path in the 2025 v1 DFN is associated with interaction between the hydraulic fracture and natural fractures that limits further fracture propagation during Stage 10. The interactions between the hydraulic and pre-existing natural fractures forming the two common flow paths differ between the two DFN realizations and are more complex in the 2025 v1 DFN.

Fiber-optic measurements recorded during Stage 10 indicate a fracture hit at a location approximately above the Stage 10 perforation cluster. This observation suggests limitations in the 2025 v1 DFN realization, uncertainties in fracture mechanical or hydraulic properties, or a combination of both.

To further explain the Stage 10 response, Figure 14 shows a zoomed-in view of the aperture distribution for the 2025 v1 DFN impermeable scenario at the point reached in the simulations during Stage 10. Several small intersecting natural fractures are located in the immediate vicinity of the perforation cluster. One of these fractures is moderately dipping and unfavorably oriented with respect to the maximum principal stress (Sv in a normal-faulting regime), causing it to act as a barrier to hydraulic fracture propagation. The hydraulic fracture generated during Stage 10 merges downwards with the natural fracture reactivated in Stage 9, while its upward propagation is completely arrested.

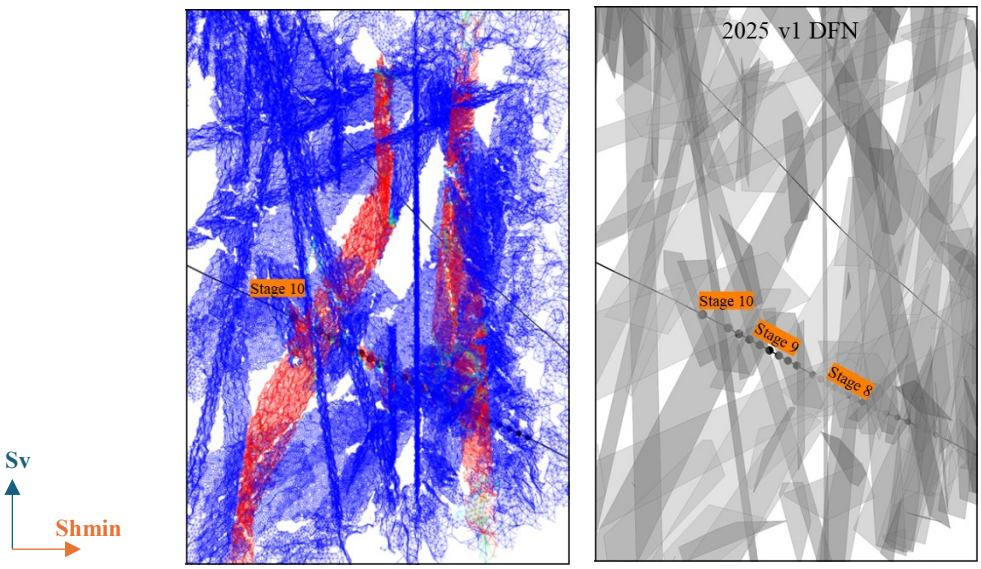

Figure 14: Zoomed-in view of the aperture distribution around Stage 10 for the 2025 v1 DFN impermeable scenario at the simulated state reached during Stage 10 (left). (Right) The 2025 v1 DFN in the vicinity of Stage 10.

3. CONCLUSION

This study investigated the influence of DFN characteristics on hydraulic stimulation at the Utah FORGE site using coupled hydro-mechanical modeling in XSite.

Due to discrepancies in previous modeling efforts in DFN hydromechanical properties needed to reproduce recorded field data and the update of the DFN geometry, this paper first conducted a sensitivity analysis of key hydraulic and mechanical properties to assess the impact on reservoir response to stimulation. This analysis used Stage 1 of the 2022 hydraulic stimulation campaign with the latest DFN realization and focused on identifying properties that best reproduce the injection pressure history and recorded microseismic events. The results show that the predicted stimulation mechanism and reservoir response to fluid injection are greatly influenced by the DFN's spatial distribution, density, and connectivity. While previous modeling efforts concluded that an initially permeable DFN without cohesive strength provided the best match to field data, the results show that this no longer holds for the updated DFN realization constrained with additional datasets (2025 v1 DFN). In particular, the initially permeable DFN results in a highly diffusive response with shear slip events far from the injection point. Recorded microseismic event locations from Stage 1 do not support this. The sensitivity analysis shows that the best match to Stage 1 field data with the latest DFN realization is one with initially impermeable fractures and moderate shear strength. This combination of properties generally reproduces the extent of microseismic events and observed injection pressure history.

The calibrated modeling framework was then applied to stimulation Stages 8–10 of the 2024 campaign. The simulations were performed using both the 2024 DFN realization and the newly developed 2025 v1 DFN realization. For each DFN realization, two fracture hydromechanical property cases were considered: a strong impermeable DFN case and a weak permeable DFN. For the impermeable DFN cases, both realizations yield similar bottomhole pressure predictions for Stages 8 and 9. In contrast, for Stage 10 the 2025 v1 DFN significantly overestimates the field pressure response, which is attributed to interaction with natural fractures that limit hydraulic fracture propagation in the vicinity of the perforation cluster. The permeable DFN cases tend to underestimate the pressure response, particularly for the 2025 v1 DFN, due to increased hydraulic diffusivity of a denser and more connected fracture network. In terms of microseismicity, that shear reactivation is the dominant stimulation mechanism in the 2025 v1 DFN, whereas the 2024 DFN allows for more localized tensile fracture development for DFN impermeable conditions. While neither DFN realization fully reproduces the observed microseismic activity along the major fault F2, the updated DFN yields a more diffuse shear event distribution that is spatially closer to the observed microseismic cloud. Overall, permeable DFN scenarios overestimate the spatial extent of simulated microseismicity, while impermeable DFN scenarios provide a closer match to the observed event extent. Sensitivity analysis using Stage 1 of the 2022 stimulation identified an initially impermeable DFN with reduced shear strength as providing the best match to field data; evaluating whether this parameterization also applies to Stages 8–10 remains to be done.

This study adopts several simplifying assumptions. Fractures are assumed to have uniform hydromechanical properties (independent of the fracture size), whereas, in reality, these properties are variable within a DFN (and probably correlated to the fracture size). For example, all fractures are assigned the same shear strength and stiffness, neglecting potential variability associated with fracture size and orientation. Fracture apertures are also prescribed using a single aperture-length relation uniformly across the DFN. While these assumptions allow for controlled comparison between DFN realizations, they may oversimplify the hydromechanical response and contribute to discrepancies observed in some stages.
Finally, the strong sensitivity of the stimulation response to local DFN geometry, especially near Stage 10, suggests that key fracture features may still be missing or misrepresented. Improved characterization of this region, combined with adjusted mechanical properties, may help reproduce the observed microseismic activity along Fault F2 in future simulations.

ACKNOWLEDGEMENTS

Funding for this work was provided by the U.S. Department of Energy under grant DE-EE0007080 "Enhanced Geothermal System Concept Testing and Development at the Milford City, Utah FORGE Site." We thank the many stakeholders supporting this project, including Smithfield, Utah School and Institutional Trust Lands Administration, and Beaver County, as well as the Utah Governor's Office of Energy Development.

This research made use of the resources of the High Performance Computing Center at Idaho National Laboratory, which is supported by the Office of Nuclear Energy of the U.S. Department of Energy and the Nuclear Science User Facilities under Contract No. DE-AC07-05ID14517.

REFERENCES

Ajo-Franklin. J., Correa, J., Freifeld, B., Becker, M., Ghassemi, A. & Coleman, T.: Final Report for Fiber-Optic Geophysical Monitoring of Reservoir Evolution at the Utah FORGE. Final Technical Report (2025).

Damjanac, B., & Cundall, P.: Application of Distinct Element Methods to Simulation of Hydraulic Fracturing in Naturally Fractured Reservoirs, Computers and Geotechnics, 71, (2016), 283–294. https://doi.org/10.1016/j.compgeo.2015.06.007

Dyer, B., Karvounis, D., Meier, P., Fiori, R., & Jaques, P.: Utah FORGE: GES Well 16A(78)-32 and Well 16B(78)-32 Stimulation Seismic Event Catalogs, (2024). https://doi.org/10.15121/2455012

Finnila, A., Doe1, T., Podgorney, R., Damjanac, B. and Xing, P.: Revisions to the Discrete Fracture Network Model at Utah FORGE Site, Proceedings, Geothermal Rising Conference: Using the Earth to Save the Earth, GRC 2021, San Diego, CA (2021).

Finnila, A., and Jones, C.: Updated Reference Discrete Fracture Network Model at Utah FORGE, Proceedings, 49th Workshop on Geothermal Reservoir Engineering, Stanford University, Stanford, CA (2024).

Finnila, A. (2025). Utah FORGE: Updated Discrete Fracture Network Model – 2025 [Dataset]. GDR, WSP Golder.

Fu, W., Damjanac, B., Radakovic-Guzina, Z., Finnila, A., Podgorney, R. and Mclennan, J.: Near-Wellbore DEM Model of Hydraulic Fracture Initiation for Utah FORGE Site, Proceedings, 49th Workshop on Geothermal Reservoir Engineering Stanford University, Stanford, CA (2024).

Fu, W., Savitski, A. A., Damjanac, B., & Bunger, A. P.: Three-Dimensional Lattice Simulation of Hydraulic Fracture Interaction with Natural Fractures, Computers and Geotechnics, 107, (2019). 214–234. https://doi.org/10.1016/j.compgeo.2018.11.023

Fu, W., Ames, B. C., Bunger, A. P., & Savitski, A. A.: Impact of Partially Cemented and Non-persistent Natural Fractures on Hydraulic Fracture Propagation, Rock Mechanics and Rock Engineering, 49(11), (2016), 4519–4526. https://doi.org/10.1007/s00603-016-1103-0

Ghassemi, A., Ye, Z., Lee, S. H. & Ajo-Franklin, J. (2025). Fluid flow, Rock Deformation, and Seismic Response During Utah FORGE Circulation Tests. Presented at the 50th Workshop on Geothermal Reservoir Engineering, Stanford, CA.

Itasca: XSite-Hydraulic Fracture Simulation of 3D Fracture Networks (4.0), Minneapolis, Minnesota (2023).

Klimczak, C., Schultz, R.A., Parashar, R. and Reeves, D.M. (2010). Cubic law with aperture-length correlation: implications for network scale fluid flow, Hydrogeology journal, 18(4), pp.851-862.

McLennan, J., England, K., Rose, P., Moore, J., & Barker, B. (2023). Stimulation of a high-temperature granitic reservoir at the Utah FORGE site. SPE hydraulic fracturing technology conference and exhibition.

McLennan, J., Swearingen, L., and England, K.: Utah FORGE: Wells 16A(78)-32 and 16B(78)-32 Stimulation Program Report - May 2024, (2024). https://doi.org/10.15121/2483880

Niemz, P., Pankow, K., Isken, M., Whidden, W., McLennan, J. and Moore, J.: Mapping Fracture Zones with Nodal Geophone Patches: Insights from Induced Microseismicity During the 2024 Stimulations at Utah FORGE, Seismological Research Letters, (2025). https://doi.org/10.1785/0220240300

Podgorney, R., Munday, L., & Finnila, A. (2025). Thermo-Hydraulic Modeling of Long-Term Circulation Tests at the Utah FORGE Site. Presented at the 50th Workshop on Geothermal Reservoir Engineering, Stanford, CA.

Tounsi, H., Damjanac, B., Radakovic-Guzina, Z., Fu, W. Finnila, A., Xing, P. and Podgorney, R. (2025a). A Coupled Hydro-Mechanical Analysis of Impact of DFN on Reservoir Stimulation at FORGE. Presented at the 50th Workshop on Geothermal Reservoir Engineering, Stanford, CA.

Tounsi, H., Damjanac, B., Radakovic-Guzina, Z., Fu, W., Finnila, A., Xing, P., ... & McLennan, J. (2025b). Influence of Natural Fractures on Hydraulic Stimulation in Geothermal Reservoirs: Insights from Utah FORGE Coupled Hydro-Mechanical Modeling. *SPE/AAPG/SEG* Unconventional Resources Technology Conference.

Xing, P., Damjanac, B., Radakovic-Guzina, Z., Torres, M., Finnila, A., Podgorney, R., Moore, J. and McLennan, J.: Comparison of Modeling Results with Data Recorded During Field Stimulations at Utah FORGE Site, Proceedings, 48th Workshop on Geothermal Reservoir Engineering, Stanford, CA (2023).

Xing, P., England, K., Moore, J. & McLennan, J. Analysis of the 2024 Circulation Tests at Utah FORGE and the Response of Fiber Optic Sensing Data (2025). Presented at the 50th Workshop on Geothermal Reservoir Engineering, Stanford, CA.